



Effects of fluvial instability on the bed morphology in vegetated channels

Nadia Penna¹ · Francesco Coscarella¹ · Antonino D'Ippolito¹ · Roberto Gaudio¹

Received: 31 October 2021 / Accepted: 7 January 2022 / Published online: 24 January 2022
© The Author(s) 2022

Abstract

Flume experiments are conducted to investigate the effect of streambed instability in channels with randomly-distributed vegetation, varying vegetation density and flow conditions, in the absence of upstream sediment supply. The bed morphology is captured with the photogrammetry technique and a Laser Scanner, and its changes with the vegetation and flow conditions are investigated. The results demonstrate that the presence of vegetation contributes in promoting the stability of the streambed and the formation of multiple bars. In runs with low vegetation density, the trajectory of sediment transport is predominantly in the longitudinal direction. However, a slight lateral dispersion of sediments is observed in the run with low flow discharge. By increasing the vegetation density, the bed structures become shorter, with a lower wavelength, than before, but with a similar trend. The analysis of the energy spectra and the high-order generalized structure functions of bed elevation fluctuations demonstrates that the bed surfaces are monofractals and can be described by a single exponent. However, the runs affected also by a lateral dispersion of sediments during the sediment transport phase are characterized by multifractality, which implies that a complex bed morphology at small spatial lags occurs at the end of these runs. The study of the two-dimensional (2D) second-order structure functions demonstrates that the bed is characterized by an anisotropic behavior, with flow-aligned bed structures that reflect the way in which the bed was formed.

Article Highlights

- Vegetation contributes in promoting the stability of the streambed
- Multiple bars are formed in vegetated channels with different wavelengths, depending on the flow and the vegetation density conditions
- Bed surfaces in the presence of vegetation are monofractals, except those in which lateral sediment transport occurs

✉ Roberto Gaudio
gaudio@unical.it

¹ Dipartimento di Ingegneria Civile, Università Della Calabria, CS 87036 Rende, Italy

Keyword Vegetated flows · Sediment transport · Bed morphology structures · High-order structure functions

List of Symbols

a	Frontal area per volume
B	Flume width
C	Intermittency parameter
d	Cylinder diameter
d_{16}	16% (by weight) finer size of sand
d_{50}	Median sediment size of sand
d_{84}	84% (by weight) finer size of sand
F	Froude number
g	Gravitational acceleration
g_s	Sediment transport rate
H	Hurst coefficient
h	Flow depth
h_c	Cylinder height
k	Wave number
l_x	Sampling length in the x direction
l_y	Sampling length in the y direction
M	Total number of grid points in y direction
N	Total number of grid points in x direction
n	Number of cylinders per bed area
p	Order of moments of structure functions
Q	Flow discharge
R^2	Coefficient of determination
Re	Reynolds number
Re_d	Reynolds number of the vegetation stem
Re_*	Shear Reynolds number
r	Number of samples in the x direction
S	Streamwise bed slope
S_p	Structure function of p -order
s	Number of samples in the y direction
T	Total duration of the experimental run
t	Time
U	Approaching average flow velocity
U_c	Threshold streamwise velocity
u_*	Shear velocity
x	Streamwise coordinate
y	Spanwise coordinate
z	Vertical coordinate
α	Coefficient of the sediment transport rate equation
β	Exponent of the sediment transport rate equation
δx	Sampling interval in the x direction
δy	Sampling interval in the y direction
ε	Nikuradse equivalent sand roughness
θ	Shields mobility parameter
ν	Coefficient of kinematic viscosity of water

ξ_p	Scaling exponent
σ_g	Geometric standard deviation of the grain size distribution
φ	Solid volume fraction occupied by the canopy elements

1 Introduction

Alterations in the flow conditions of a river may lead to instability of the streambed [1]. Specifically, instability occurs when the flow interacts with a movable boundary, modeling its planform morphology [2] and its elevation. Streambed instability may occur at different spatiotemporal scales [3] depending on the cause that gives rise to the phenomenon. In fact, rivers may not always respond progressively to altered conditions [4]. For example, stream restoration projects usually involve some modifications to the channel or the banks, which have consequences on the river flow conditions that are effective in months or years. Rather, dramatic morphologic changes can occur abruptly when critical flow discharges are exceeded [5].

In general, the bed morphology changes resulting from streambed instability can be classified as small-, meso-, or large-scale changes, mainly depending on their characteristic wavelengths [1, 3]. However, different spatial scales may coexist in the same pattern [3]. These scales should be identified and separated in order to be characterized in relation to the cause that generated them. Meandering, braiding, bedform formation are just three examples of the patterns that can result from the interaction between flow and sediment transport [2, 3].

Many research works were focused on streambed instabilities, addressing significant aspects, such as the development of bedforms and their stability [6], ripple and dune dynamics [7], the differences between free and forced fluvial patterns [3], and many others that are not listed for brevity. However, very recently, Dey and Ali [1] in their review work on fluvial instabilities have outlined the current research challenges of the subject. Among them, they highlighted the need to effectively include the role of vegetation in the analytical models of the instability analysis to further explore the mechanisms of meso- and macro-scale fluvial instabilities.

Indeed, the bed of an active channel can be characterized by other roughness elements besides bed sediments, that is vegetation of different shape, roughness and bending stiffness (trees, lush shrubs and grasses of different species) [8, 9]. Aquatic vegetation may have a strong impact on the erosion and sediment transport processes [10, 11], affecting the streambed instability and the river morphology. If on one hand a great amount of work has been focused on the identification of the coherent flow structures induced by the flow-vegetation interactions (also in the presence of a rough and fixed bed) [12–15], on the other less experimental works were carried out considering the interactions between flow, vegetation and mobile beds [16–18]. In the studies on bedload transport in vegetated flows, however, the experimental runs were conducted in flumes with emergent rigid vegetation simulated by using circular cylinders having uniform size and homogeneous distribution [19–21].

From the literature review, no experimental works on sediment transport were found with non-uniformly vegetated beds or with a random vegetation distribution. Hitherto, such a phenomenon seems to have received inadequate attention, although it represents a crucial aspect for the instability analysis of a streambed.

Therefore, the aim of the present study is to examine the effect on morphology of streambed instability in vegetated channels, considering vegetation with random distribution. Specifically, starting from an initial condition in which the bed is stable, owing to an increase in the flow discharge and the presence of vegetation, bed instability is induced. Two different perturbations in the experimental conditions are considered in this study: (1) a change in vegetation density; (2) a further increase in the flow discharge.

Thus, the manuscript is organized as follows: first, the experimental setup and the procedure used for the execution of the experimental runs are illustrated, together with the methodology adopted for the acquisition of the bed morphology. This section is followed by the description of the bed elevation data processing. In Sect. 4, the results are presented and discussed in terms of: (1) the effects of vegetation on the sediment transport process; (2) the bed morphology at the equilibrium stage; (3) the statistics of the bed morphology, which includes the analysis of the energy spectra and of the high-order structure functions of bed elevations data. Finally, in Sect. 5, the findings of the present study are summarized.

2 Experimental setup

The laboratory experimental runs were conducted in a recirculating hydraulic tilting flume at the *Laboratorio “Grandi Modelli Idraulici”, Università della Calabria, Italy* (see Fig. 1 for the schematic of the experimental setup). The dimensions of the rectangular flume were 9.6 m in length, 0.485 m in width and 0.5 m in height. The flume had a 7 m-long, 12 cm-deep recess box located 1 m downstream of the flume inlet. The study area for the experiments was set 6.0 m downstream of the inlet and was 2.0 m in length. The coordinate system used in this study is three-dimensional (x, y, z), where x, y and z are the streamwise, spanwise and vertical coordinates, respectively. The initial section of the study area is the origin of the x -axis lying on the bed, as shown in Fig. 1.

The emergent rigid vegetation was replicated with randomly arranged vertical, wooden and circular cylinders, having the following sizes: 0.02 m in diameter, d , and 0.40 m in height, h_c . Each cylinder was inserted into a 1.96 m-long, 0.485 m-wide and 0.015 m-thick Plexiglas panel fixed to the channel bottom, starting from the abscissa $x = -0.22$ m.

The bed was created by using uniform very coarse sand having a median diameter $d_{50} = 1.53$ mm, with a geometric standard deviation $\sigma_g = (d_{84}/d_{16})^{0.5} < 1.5$ [22], where d_{16} and d_{84} are the sediment sizes for which 16% and 84% by weight of sediment is finer, respectively. The longitudinal bottom slope of the flume, S , was fixed at 1.5‰ by maneuvering a hydraulic jack.

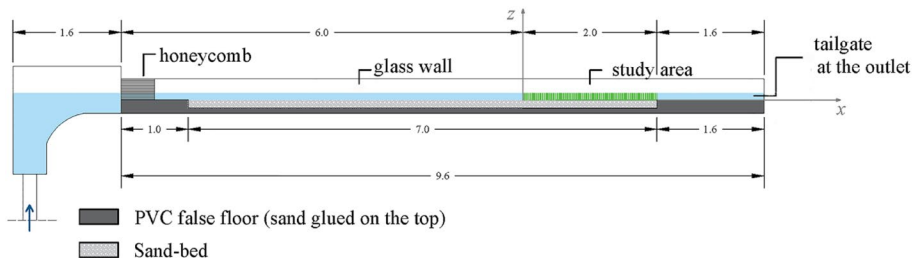


Fig. 1 Side view of the experimental facility (dimensions are expressed in meters)

The flume was filled in with freshwater at a temperature of 20°C, and kinematic viscosity $\nu = 10^{-6} \text{ m}^2 \text{ s}^{-1}$. The flow was supplied with an electric pump. To suppress the disturbance of the pump on the turbulence characteristics of the flow, flow straighteners made of honeycombs (10 mm in diameter) were installed at the flume inlet. The discharge was controlled by a valve and measured by a V-notch weir fixed in a downstream tank, located upstream of the restitution channel. A point gauge with a decimal Vernier, having an accuracy of $\pm 0.1 \text{ mm}$, was installed to measure the water depth, h , within the flume at $x=0$. At the outlet, a tailgate to regulate the water depth was mounted.

To study the streambed instability in vegetated channels, six runs were conducted, considering two different perturbations in the experimental conditions: a change in (1) vegetation density and (2) flow discharge. The hydraulic parameters of each run are provided in Table 1. The name of the runs recalls the adopted experimental conditions (for instance, run R1B stands for flow discharge 1 equal to $Q = 11.85 \text{ l s}^{-1}$ and vegetation density of type B with 34 vegetation stems). Note that runs R1A and R2A were conducted without vegetation as benchmarks for the other tests, which were, instead, characterized by two different vegetation densities. Specifically, runs identified by the letter “B” refer to a total number of 34 cylinders randomly arranged [Fig. 2a], with a frontal area per volume $a = nd = 0.71 \text{ m}^{-1}$, where $n = 36 \text{ m}^{-2}$ was the number of cylinders per bed area, while the solid volume fraction occupied by the canopy elements was $\varphi = \pi ad/4 = 0.01$. Runs B refer to the condition of vegetation with moderate density, whereas Runs C were denoted by 68 cylinders randomly arranged [Fig. 2b], with $n = 72 \text{ m}^{-2}$, $a = 1.43 \text{ m}^{-1}$ and $\varphi = 0.02$. Hence, runs C correspond to the condition of high-density vegetation. In both the cases, the random distributions used in the flume were generated by an original algorithm programmed with *MatLab*.

Along with the aforementioned quantities, the following hydraulic parameters are listed in Table 1: the approaching average flow velocity, $U [= Q/(Bh)$, where B is the flume width]; the critical flow velocity for the initiation of sediment motion, U_c ; the shear velocity estimated from $u_* = (ghS)^{0.5}$, where g is the gravitational acceleration; the flow Froude number, $F [= U/(gh)^{0.5}]$; the flow Reynolds number, $Re (= 4Uh/\nu)$; the Reynolds number of the vegetation stems $Re_d (= Udl/\nu)$; and the shear Reynolds number $Re_* (= u_*\varepsilon/\nu$, where ε is the Nikuradse equivalent sand roughness, equal to about $2d_{50}$). The critical velocity for the inception of sediment motion U_c was determined through the Neill formula [23], as follows:

$$U_c = 31.08\theta^{1/2}h^{1/6}d_{50}^{1/3} \quad (1)$$

where θ is the Shields mobility parameter, computed on the basis of the sediment size [24].

It is possible to note that, as expected, the water depth increases with the vegetation density, from R1A to R1C and from R2A to R2C, causing a slight decrease in the flow velocity. All the experiments were performed in live-bed condition (with flow intensity $U/U_c > 1$), keeping the flow discharge constant in each series R1 and R2, since the study aimed at evaluating the response of the bed morphology and its stability to a change in flow conditions and vegetation density. Furthermore, the runs were all conducted in sub-critical flow conditions ($F < 1$) and rough-turbulent regime ($Re_* > 70$).

3 Experimental procedure

The procedure adopted for each experimental run is described in details below.

Table 1 Hydraulic parameters of the experimental runs

Run	No. of stems	Q (l s^{-1})	h (cm)	U (m s^{-1})	U_c (m s^{-1})	U/U_c	u_* (m s^{-1})	F	Re	Re_d	Re_*
R1A	–	11.85	5.40	0.452	0.383	1.18	0.028	0.622	97,731	9049	86
R1B	34	11.85	5.60	0.436	0.386	1.13	0.029	0.589	97,731	8726	88
R1C	68	11.85	6.00	0.407	0.390	1.04	0.030	0.531	97,731	8144	91
R2A	–	19.85	6.25	0.655	0.393	1.67	0.030	0.836	163,711	13,097	93
R2B	34	19.85	7.20	0.568	0.402	1.41	0.033	0.676	163,711	11,369	100
R2C	68	19.85	8.50	0.481	0.413	1.16	0.035	0.527	163,711	9630	108

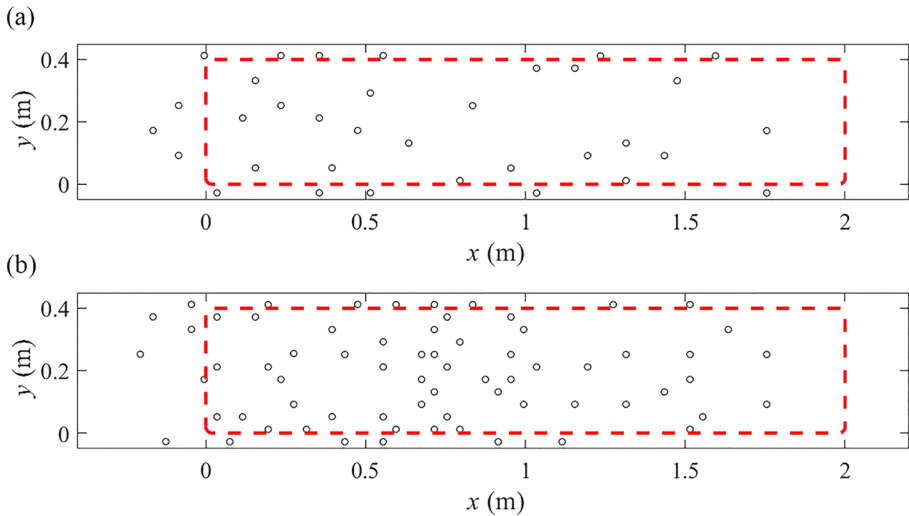


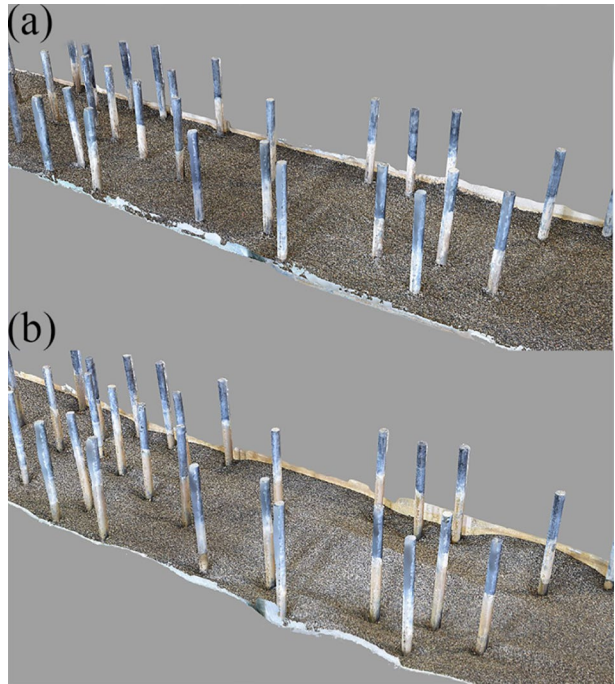
Fig. 2 Top view of the cylinder arrays in the laboratory flume: **a** vegetation density of type B (34 cylinders), and **b** vegetation density of type C (68 cylinders). The red dashed rectangle delimitates the study area having a length of 2 m and a width of 0.4 m. The origin of the y -axis is located 0.05 m from the right flume wall looking downstream

Before starting the run, the bed was prepared by randomly depositing and screeding wet sand into the flume, to ensure the same slope of the flume bottom. Then, the bed surface topography was acquired with the photogrammetry technique. This methodology is based on the acquisition of several photographs of a specified object from different locations, orienting the camera downwards at an angle of about 45° . In this study, a Nikon D5200 camera, equipped with the Nikkor 18–55 mm $f/3.5$ –5.6G VR lens, was employed. The photographs covered a flume area with a total length of 2 m and width of 0.4 m, which corresponds to the study area shown in Fig. 2. The software *Metashape* (Agisoft) was used to align the photographs, to build a three-dimensional (3D) point cloud and, finally, to reconstruct an unstructured triangular mesh representing the bed surface. The alignment was done through the recognition from the photographs of the targets placed on the flume walls. Then, the flume was scanned by using a Terrestrial Laser Scanner (TLS, Leica ScanStation P20). The data from the TLS was processed using the manufacturer's software, *Cyclone* 9.0 (Leica Geosystems), in order to scale the unstructured triangular mesh obtained from the photogrammetry technique. Subsequently, using the commercial software *Rhinoceros* (McNeel & Associates), a structured grid was extracted with a spatial resolution of 2 mm in both the streamwise and spanwise directions.

After this initial step, maneuvering the tailgate to prevent any sediment motion, the flume was slowly filled in with water. Thus, the pump was turned on and a flow discharge of about 2 l s^{-1} was supplied at the inlet, lowering the tailgate completely. This flow exerted a shear stress on the surface of the bed grains, which evidently was much smaller than its threshold limit, as the grains maintained a stable equilibrium. The acquired initial bed surface represents the bed surface below the threshold limit. As an example, Fig. 3a shows the unstructured triangular mesh of the initial bed surface of run R1B.

The run effectively started when an increase in the flow discharge was applied (i.e., of about 10 l s^{-1} and 18 l s^{-1} for runs R1 and R2, respectively). The plane bed became

Fig. 3 Unstructured triangular meshes of the **a** initial and **b** final bed surfaces of run R1B



unstable, owing to the motion of grains at the bed surface, which means that the threshold shear stress was exceeded. Note that no sediment feeding was supplied at the flume inlet. Therefore, the sediment transport originated solely from the erosive action of the flow, which causes bed instability. The sand, evacuated from the flume, was collected in a sediment trap placed in the downstream tank. The sediment transport rate was measured at different time intervals by weighing the collected sediments after having drained the water out. Thus, the run was stopped when the transport rate dropped down to less than 1% of the initial rate.

At the end of this process, the pump was turned off and the flume was slowly emptied without any disturbance to the bed topography, by using a bottom outlet located at the end of the study area ($x = 1.8$ m). Hence, the 3D bed surface topography was acquired again with the photogrammetry technique. Therefore, the final bed surface represents the result of the interplay between the flowing discharge and the erodible boundary at their interface. As a comparison between the bed surfaces before and after the sediment transport process, Fig. 3b shows the unstructured triangular mesh of the final bed surface of run R1B.

4 Bed elevation data processing

Each structured grid was characterized by a total number of $N \times M = 200,000$ points, where $N = 1,000$ points in the streamwise direction and $M = 200$ points in the spanwise direction, with a space resolution of 2 mm. A bilinear detrending algorithm was applied to the structured grids to remove the respective surface bed slopes, which could obscure the bed surface properties [25].

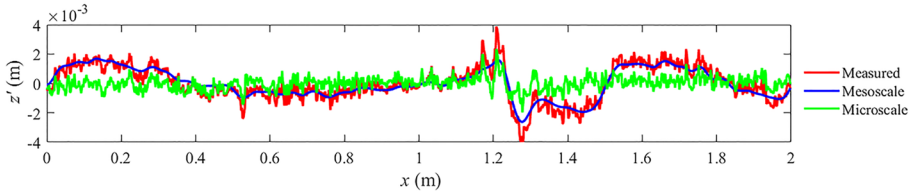


Fig. 4 Example of comparison among the same longitudinal bed profile in the measured, mesoscale and microscale grids

Table 2 Summary of sediment transport results

Run	T (h)	Total sediment weight (kg)	α	β	R^2 (%)
R1A	124	190	0.009	-0.51	93.2
R1B	117	155	0.010	-0.59	91.1
R1C	74	124	0.011	-0.59	88.6
R2A	46	311	0.043	-0.71	93.5
R2B	46	159	0.047	-1.44	99.7
R2C	76	142	0.067	-2.21	99.9

Subsequently, the mean bed elevation \bar{z} was subtracted from the bed elevation data of each detrended structured grid, in order to have a zero-mean bed elevation. This new grid is henceforth called *measured* grid and is characterized by elevation data in terms of fluctuations z' of z with respect to \bar{z} .

To distinguish the different spatial scales of the bed topography, the surfaces at the meso- and micro-scale were extracted from the measured grids. Specifically, the *mesoscale* surface was a trend surface fitted to a regular grid with point spacing equal to 1.6 cm ($\sim 10 d_{50}$). The elevation of grid points was determined by averaging the measured elevations within a square of $1.6 \times 1.6 \text{ cm}^2$ centered on the grid point. A bicubic spline was applied to interpolate between the grid points at the location of the measured grid [26]. Various space resolutions were tested before reaching this final configuration, increasing the distance between the grid points. The final grid allowed describing adequately the undulation of the mesoscale topography. Finally, subtracting the mesoscale grid from the measured grid, the *microscale* grid was determined, that is the topography due to sediment grains [27]. As an example, Fig. 4 shows the comparison between the three different grids referred to the same longitudinal profile. Note that this study was mainly concentrated on the analysis of the measured and mesoscale grids, since the effect of vegetation on the bed morphology is principally evident and prominent at the mesoscale.

5 Results and discussion

5.1 Effects of vegetation on the sediment transport process

The sediment transport rate, g_s , during the experimental runs was evaluated at different time intervals. Tab. 2 shows the total duration of each run T and the total weight of the sediment collected at the flume outlet. It is evident that the bed morphology took more time to

reach equilibrium in runs R1A and R1B than in runs R2A and R2B, respectively. On the contrary, for the case of very dense vegetation (68 cylinders), the duration is almost constant, regardless of the flow discharge. At the same time, the effect of vegetation on sediment transport is clear considering the total sediment weight estimated at the end of the experimental runs. Vegetation causes a reduction of the total weight of sediment collected from the flume. This is also an index of a reduction in sediment transport. Specifically, keeping the flow discharge constant, a vegetation with moderate density (run R1B) retains about 18% of the total sediment weight of run R1A (without vegetation) and, considering a high-dense vegetation (run R1C), about 35% and 20% of those in run R1A and run R1B, respectively. Increasing the flow discharge, in run R2A the total sediment weight increases of about 64% of that of run R1A, whereas the increase was limited to about 3% by comparing R2B and R1B and 15% considering R2C and R1C. Finally, it was obtained a reduction of the total sediment weight of about 49% and 54% adding a moderate dense vegetation (run R2B) and a high dense vegetation (R2C), respectively, to the flow condition R2. Thus, it can be concluded that vegetation hinders the sediment transport and its effect is more noticeable increasing the flow velocity.

The experimental data on sediment transport collected over time were fitted by a power law $g_s = \alpha t^\beta$, where t is time, α is the coefficient and β the exponent of the relationship. All the coefficient and exponent values for each experimental run are given in Tab. 2, together with the coefficient of determination, R^2 . It is possible to note that R^2 is always greater than 88%, confirming the goodness of the power law in describing this phenomenon, as already demonstrated by other authors [28, 29]. Concurrently, Fig. 5 shows the corresponding curves for each experimental run. It can be observed that basically runs R1 can be described by the same equation, unlike runs R2, in which the vegetation effect is clear. It is also evident that runs R2 are characterized by higher sediment transport rates than runs R1, owing to the higher flow discharge. Analyzing Fig. 5a in detail, it is noticeable that the sediment transport for the bed instability starts with a higher rate in run R1C with respect to run R1B and even more to run R1A. This is induced by the local scour in correspondence of the stems, which occurred at the beginning of run R1C with greater magnitude than that of the general scour. This observation is also supported by run R1B, which follows

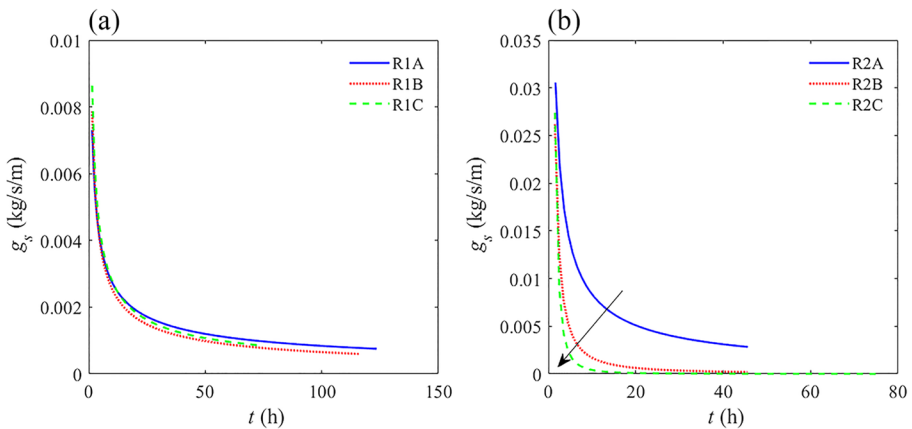


Fig. 5 Sediment transport rate, g_s , over time, t : **a** runs R1 and **b** runs R2. The black arrow indicates the decreasing behaviour of the sediment transport rate as the vegetation density increases

the same trend as that of run R1C, but with less intensity, owing to the presence of fewer cylinders. Then, the sediment transport rates quickly decrease. Runs R1B and R1C show slightly lower values than run R1A. This result fits well with the values of total sediment weights in Table 2, showing that vegetation acts as to decrease the sediment transport rate. On the other hand, runs R2 show a different behavior (Fig. 5b). Initially, in contrast to runs R1, the sediment transport rate is higher in run R2A than in the other runs with vegetation. This is due to the fact that, in this case, the flow intensity is such that the general scour represents the most important contribution to the sediment transport rate in comparison with the local scour at stems in runs R2B and R2C. Therefore, the reduction in sediment transport rate operated by the vegetation occurs immediately and is also much more evident than in the same runs with a lower flow intensity.

It can be concluded that the sediment transport process is thoroughly influenced by the presence of vegetation and its density. Specifically, it decreases as the vegetation density increases, with much more efficiency in the case of high flow intensity. Thus, it can be postulated that the presence of vegetation contributes in promoting (and not disadvantaging) the stability of the streambed.

5.2 Bed morphology at the equilibrium stage

Figures 6 and 7 shows the contour maps of the bed morphology captured before and after that the bed was eroded in the absence and presence of vegetation for the two investigated

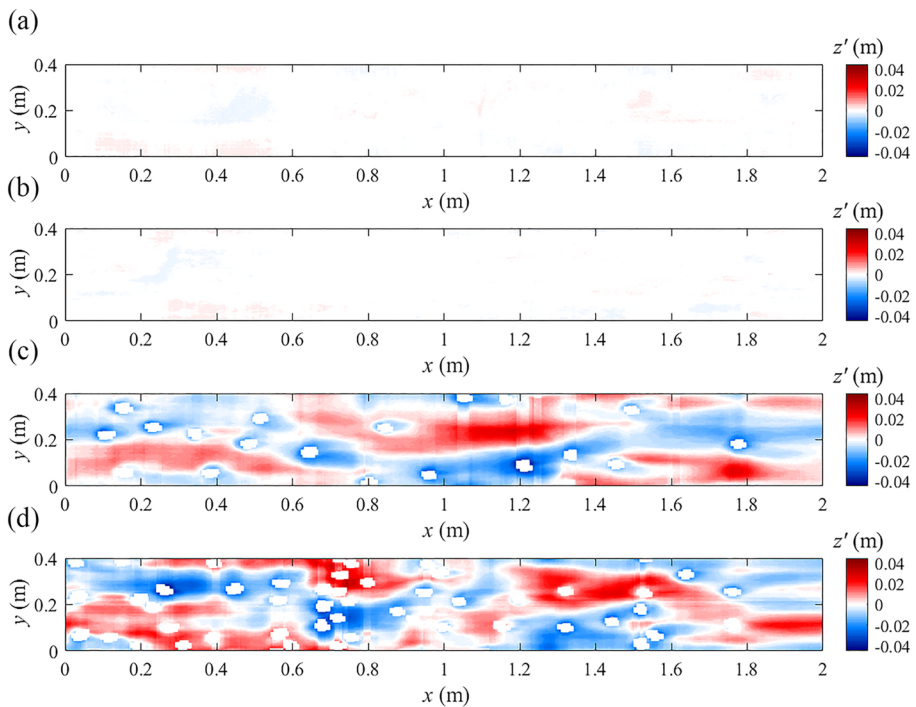


Fig. 6 Bed morphology of the study area: **a** before starting run R1A, **b** at the end of run R1A, **c** at the end of run R1B, and **d** at the end of run R1C

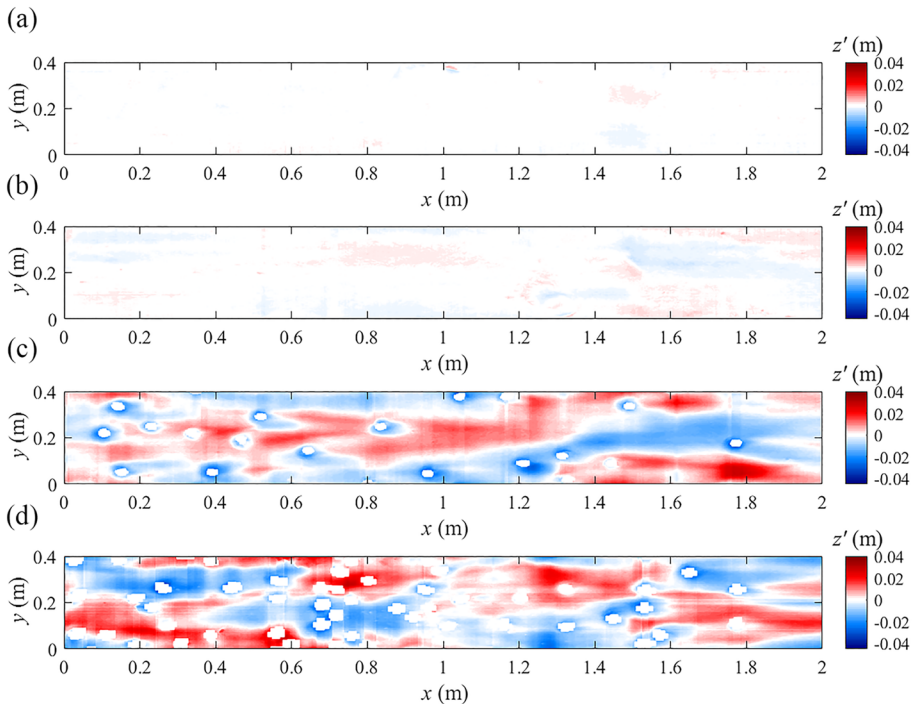


Fig. 7 Bed morphology of the study area: **a** before starting run R2A, **b** at the end of run R2A, **c** at the end of run R2B, and **d** at the end of run R2C

flow conditions, R1 and R2, respectively. Specifically, the bed morphology in the study area was represented in terms of bed fluctuations, z' .

Figures 6a and 7a refer to the initial bed condition that was later maintained with a flow discharge of about 2 l s^{-1} , during which the bed was stable. Except for very small areas with negligible positive and negative bed elevations data ($z' \sim 0$), resulting from the manual preparation of the bed before the execution of the experimental tests, it is possible to affirm that the bed was characterized by a uniform slope equal to that of the flume bottom. Thus, no bed undulations or scour holes were observed at this preliminary stage in both runs R1 and R2.

Differences on the bed morphology appear by comparing runs R1A and R2A, which are characterized by the absence of vegetation. Specifically, the weakest flow intensity of run R1A causes essentially erosion and degradation with the reduction of the bed slope, which was found to be equal to 0.7% . Thus, Fig. 6b shows a contour map with almost null bed elevation fluctuations. Instead, from the analysis of Fig. 7b, it is possible to note that the resulted bed morphology is characterized by sedimentary architectures manifested owing to the instability of the basic unperturbed flow in the straight flume [1]. This is the result of a considerable increase in the flow discharge from 2 to 19.85 l s^{-1} . Specifically, these architectures are formed by the evolutions of the bed along the streamwise and spanwise direction. In the range $0.6 < x < 1.2 \text{ m}$, a central deposition area is embedded between two lateral scour zones. Downstream, instead, in the range $1.4 < x < 2.0 \text{ m}$, the bed morphology presents a central scour area and lateral deposition zones. This configuration, being

periodic in longitudinal and transverse direction, indicates the formation of multiple bars in a movable bed and the findings are in accordance with those of Bärenbold et al. [2] in the case of unvegetated rivers.

A more complex bed morphology is visible at the end of the runs with vegetated flows. Specifically, the formation of multiple bars can be observed also in these cases. The scour corridors of Figs. 6c, d and 7c, d are the regions with intensive sediment flux, whereas the dunes indicate the trajectories of the bed-load sediments after they are entrained in the scour holes [18]. In runs R1B and R2B, both scour holes and dunes have an elongated shape along the streamwise direction, implying that the trajectory of sediment transport is predominant in the longitudinal direction (Figs. 6c and 7c). This is attributable to the low number of cylinders, such that vegetation does not deviate the sediment transport direction. However, a slight lateral dispersion of sediments can be observed in run R1B, owing to a lower flow intensity than in the latter. Furthermore, it can be noted that the erosion induced by the vegetation stems generates scour holes adjacent to the stems. By increasing the stem number, the bed structures became shorter than before and resulted to be laterally expanded. This means that very dense vegetation, as is in runs R1C and R2C, determines both longitudinal and lateral sediment transport, owing to the obstruction created by the stems. This is the reason why around some stems no scour holes are present: eroded area at the cylinders are filled in with sediments coming from upstream or laterally. The main difference between R1C and R2C is related to the height of dunes, as previously noted for

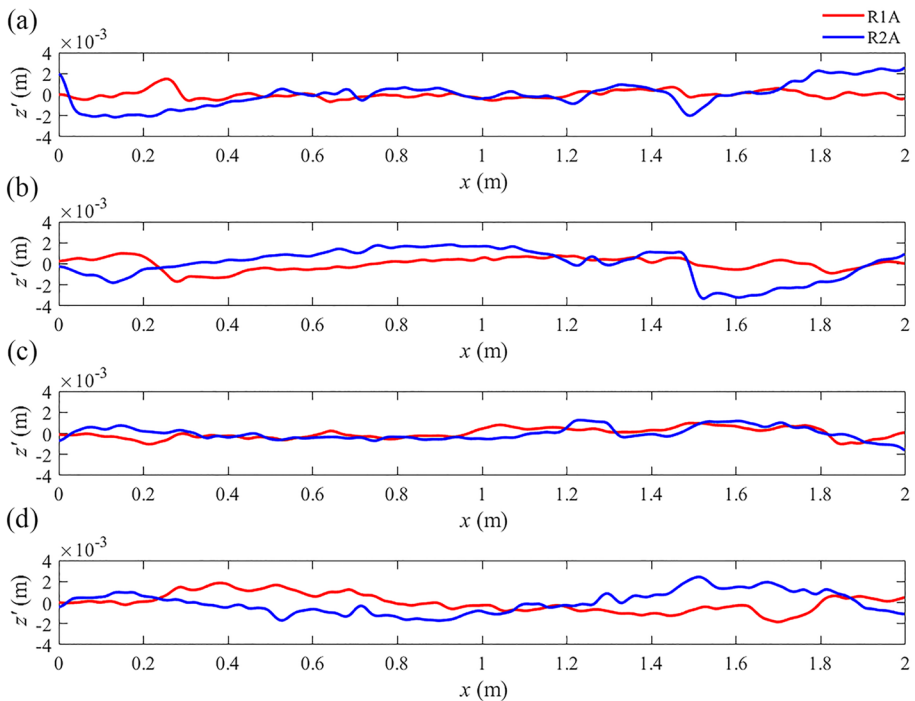


Fig. 8 Mesoscale longitudinal bed profiles of runs R1A and R2A at: **a** $y=0.35$ m, **b** $y=0.25$ m, **c** $y=0.15$ m, and **d** $y=0.05$ m

runs with vegetation of type B, which is higher for run R1C, and to a lower lateral dispersion of sediments in run R2C than in run R1C.

In order to have a clear understanding about the bed morphology, longitudinal and transverse bed profiles were extracted from the mesoscale surface. Therefore, any bed elevation variation at the grain scale was ignored, in favor of a more accurate description of the bed profiles at a larger scale. Starting from the left wall looking downstream, the longitudinal bed profiles were taken at $y=0.35, 0.25, 0.15,$ and 0.05 m, whereas the transverse bed profiles at $x=0.40, 0.80, 1.20,$ and 1.60 m.

Figure 8 shows the mesoscale longitudinal bed profiles of runs R1A and R2A. Here, the flatness of the bed in run R1A is in contrast with the undulations of the bed in run R2A, with a maximum excursion of 5 mm without considering the flume bed slope. The presence of multiple bars is evident from the comparison between the bed profiles on the left and on the right sides of the flume centerline: the deposit areas ($z' > 0$) in Figs. 8a, b correspond to scour areas ($z' < 0$) at the same abscissa in Figs. 8c, d.

Even more interesting is the comparison among the longitudinal bed profiles of runs R1B and R2B and runs R1C and R2C, which are shown in Figs. 9 and 10, respectively. By comparing the bed profiles, it is possible to note that the runs with vegetation of type C have bed undulations with shorter wavelengths and lower amplitudes than those in the runs with vegetation of type B. Unlike the unvegetated flows, the longitudinal bed profiles of vegetated flows are similar to each other considering a specific vegetation density. It is possible to note a lower wavelength in runs R2 than in runs R1, but the trend

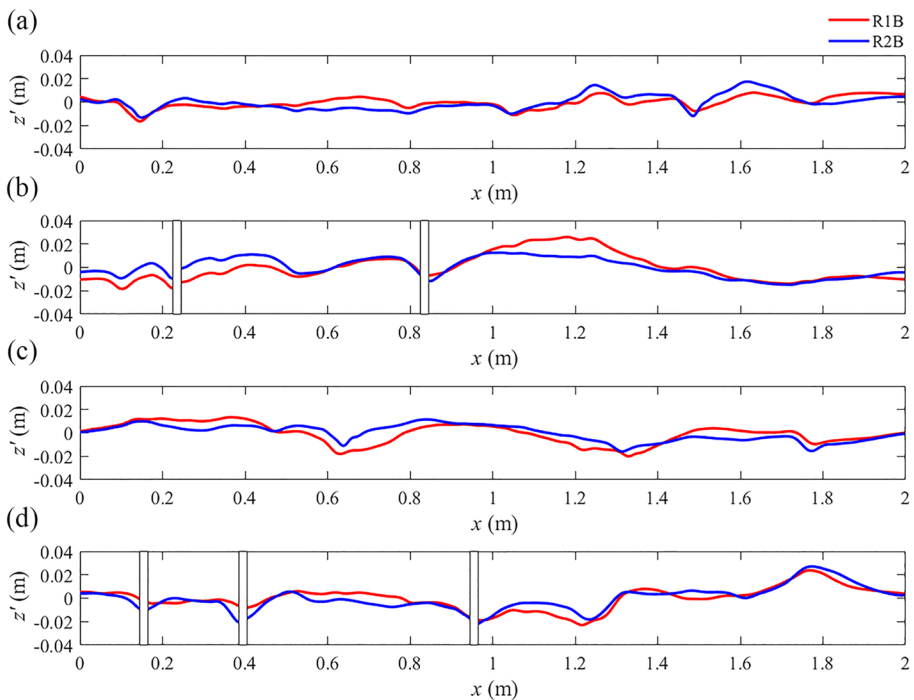


Fig. 9 Mesoscale longitudinal bed profiles of runs R1B and R2B at: **a** $y=0.35$ m, **b** $y=0.25$ m, **c** $y=0.15$ m, and **d** $y=0.05$ m

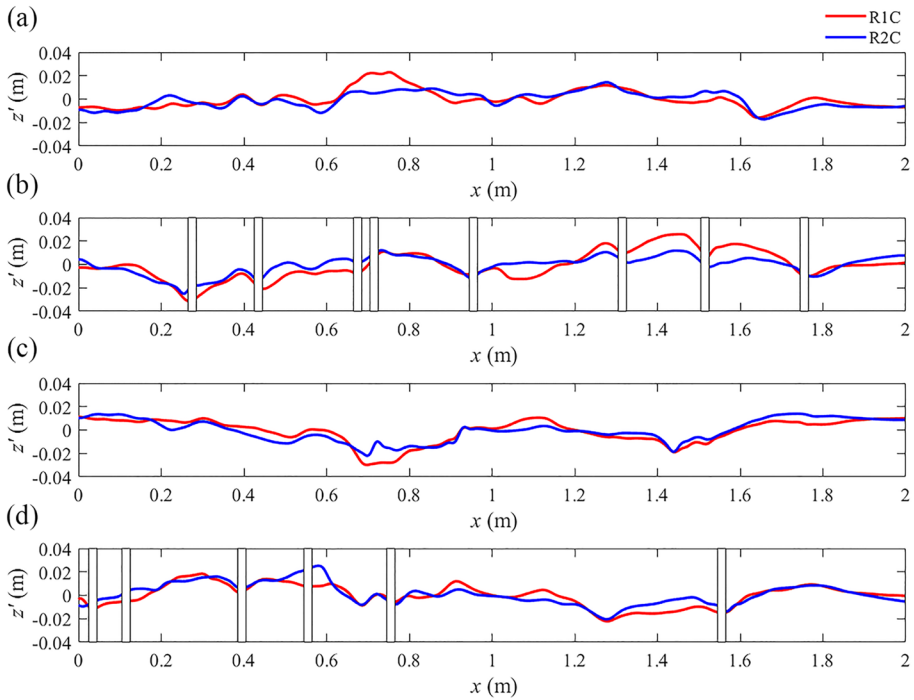


Fig. 10 Mesoscale longitudinal bed profiles of runs R1C and R2C at: **a** $y=0.35$ m, **b** $y=0.25$ m, **c** $y=0.15$ m, and **d** $y=0.05$ m

is very similar. It must be pointed out that we are comparing the bed profiles in terms of elevation fluctuations, thus, without considering of the bed degradation. What changes is the average bed elevation, which decreases as the flow discharge increases. Therefore, the fact that the longitudinal bed profiles are almost overlapped is a sign of a particular phenomenon that occurs recursively for fixed vegetation density, stem diameter and sediment diameter, regardless of the flow discharge. This latter is responsible only for the magnitude of bed degradation and not for the configuration of the bed morphology, which is instead dictated by the vegetation density and distribution. Indeed, the overlapping of the longitudinal bed profiles is more precise between runs R1C and R2C for dense vegetation. Furthermore, it is possible to note that, in general, also the maximum scour depths at the stems are similar between runs R1B and R2B and R1C and R2C, respectively. However, they are slightly higher in runs R1, owing to a flow intensity closer to unity (i.e., the threshold beyond which the clear-water condition is no longer valid and the erosion occurs with sediment transport – live bed condition, as defined by Melville and Coleman [30] for scour at bridge piers).

Finally, Figs. 11, 12, and 13 show the mesoscale transverse bed profiles in order to investigate the lateral variation of the bed morphology in runs R1A and R2A, R1B and R2B, R1C and R2C, respectively.

From the analysis of Fig. 11 the presence of multiple bars in the unvegetated flow of run R2A is demonstrated, whereas run R1A shows the flatness of the bed at each considered cross-section. For example, for run R2A, it is possible to note that the central

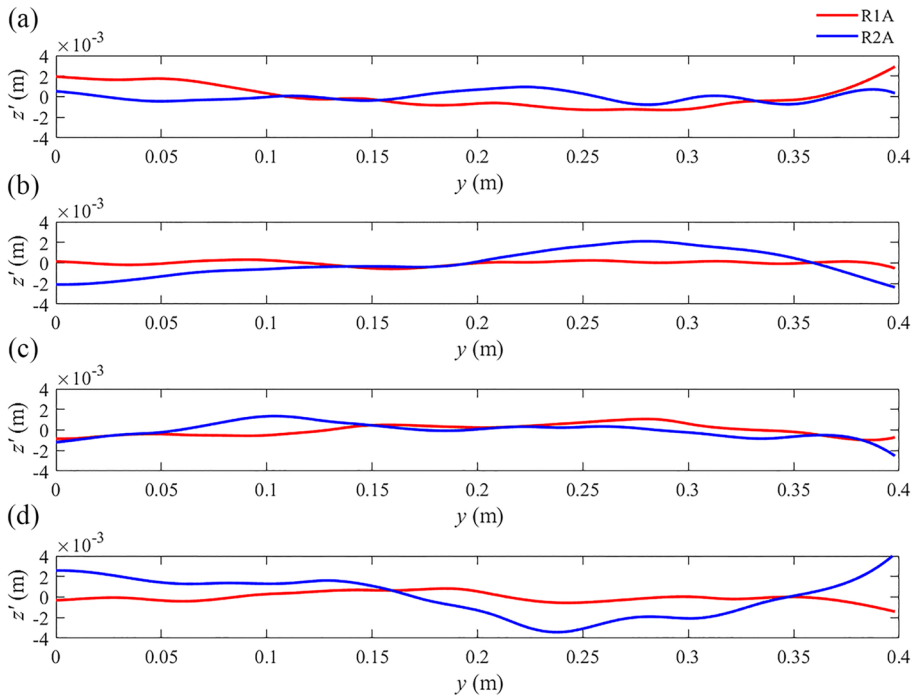


Fig. 11 Mesoscale transverse bed profiles of runs R1A and R2A at: **a** $x=0.40$ m, **b** $x=0.80$ m, **c** $x=1.20$ m, and **d** $x=1.60$ m

bar with an extension of about 15 cm ($0.20\text{ m} < y < 0.35\text{ m}$) is surrounded by two scour zones at $x=0.80$ m (Fig. 11b), and it is no longer present at $x=1.20$ m (Fig. 11c). However, downstream at $x=1.60$ m (Fig. 11d), a scour hole having a width of about 20 cm ($0.15\text{ m} < y < 0.35\text{ m}$) takes its place and is enclosed between two deposition mounds.

The transverse bed profiles of runs R1B and R2B are shown in Fig. 12. The similarity between the two cases is visible at each cross-section. The major discrepancies occur at $x=1.2$ m (Fig. 12c), where it is evident that the maximum scour depth at the stem is higher in run R1B than in run R2B. As already discussed, such behavior is due to the flow intensity of run R1B almost equal to unity, which determines erosion with low sediment transport.

Lastly, Fig. 13 illustrates the transverse bed profiles of runs R1C and R2C. In this case no relevant differences between the two runs can be noted. In particular, it appears that the bed undulations have a shorter wavelength and lower amplitude than those in the runs with vegetation of type B.

5.3 Statistics of the bed morphology

In order to further analyze the bed morphology characteristics, the bed surfaces were investigated through the energy spectra of the bed elevation fluctuations [31, 32]. The aim was to identify spectral scaling ranges, corresponding to a linear trend of the power spectrum in

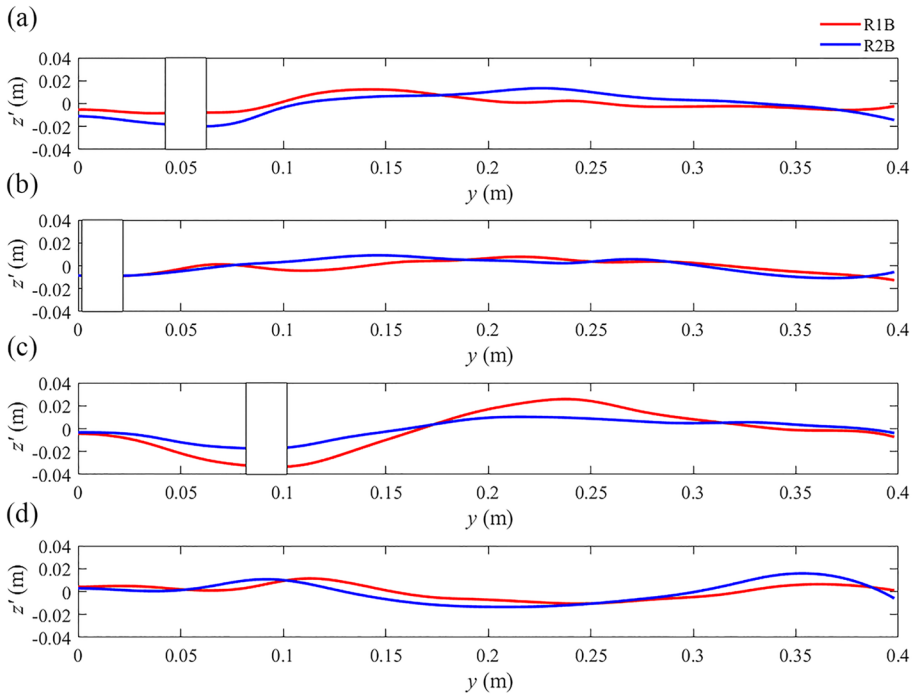


Fig. 12 Mesoscale transverse bed profiles of runs R1B and R2B at: **a** $x=0.40$ m, **b** $x=0.80$ m, **c** $x=1.20$ m, and **d** $x=1.60$ m

a log–log domain. In particular, the energy spectra were calculated for both the mesoscale and microscale surfaces in the k -space, i.e. as a function of the wave number k . The energy spectra were determined by employing the discrete fast Fourier transform of the autocorrelation function of the bed elevation fluctuations and are shown in Figs. 14 and 15 for runs R1 and R2, respectively. Specifically, Figs. 14a–c refer to the energy spectra, at the mesoscale, of the longitudinal bed elevations of runs R1A, R1B and R1C at $y=0.05, 0.15, 0.25,$ and 0.35 m, whereas Figs. 14d–f show the energy spectra of the same bed profiles at the microscale. Similarly, Figs. 15a–c illustrate the energy spectra, at the mesoscale, of the longitudinal bed elevations of runs R2A, R2B and R2C at $y=0.05, 0.15, 0.25,$ and 0.35 m, whereas Figs. 15d–f depict the energy spectra of the same bed profiles at the microscale.

From the analysis of Figs. 14a–c and 15a–c, it can be seen that spectra follow a constant power law-decay with a slope of ~ 2.00 for run R1A and R2A and ~ 2.10 for the other runs (R1B, R1C, R2B and R2C), indicating the presence of statistical scaling in the bed elevation data. The increasing of spectral slope in the vegetated flows suggests that the bed structures of comparable energy have a lower height in the absence of the stems. This finding confirms the visual observation made from the longitudinal bed profiles (Figs. 8, 9, and 10). The largest length scale of the bed structures at the mesoscale observed from these energy spectra is of the order of 30 cm for run R1A, 20 cm for run R1B and 16 cm for run R1C. Increasing the flow discharge, thus considering runs R2, the largest length scales change as follows: 50 cm for run R2A, 16 cm for run R2B and

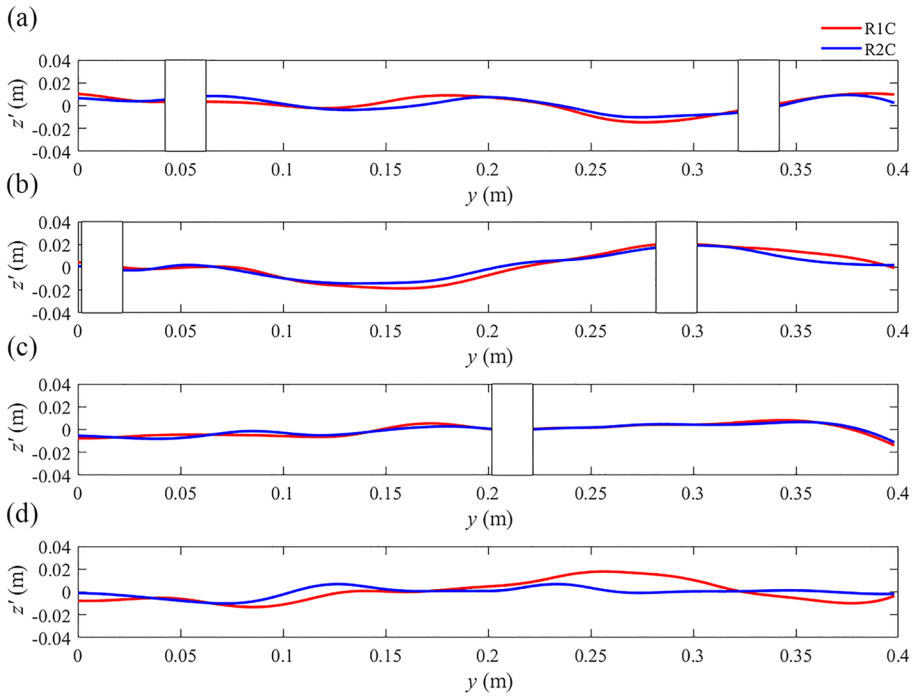


Fig. 13 Mesoscale transverse bed profiles of runs RIC and R2C at: **a** $x=0.40$ m, **b** $x=0.80$ m, **c** $x=1.20$ m, and **d** $x=1.60$ m

14 cm for run R2C. Hence, if on the one hand for the unvegetated flow the increase in the flow discharge causes a stretch of the bed structures at the mesoscale, on the other the presence of vegetation causes their contraction. The shrinking of the bed structures increases as the vegetation density increases too with the same flow rate.

By analyzing the energy spectra of the bed fluctuations at the microscale for runs R1 (Figs. 14d–f) and R2 (Figs. 15d–f), instead, it is possible to observe a net decrease in energy, which indicates a lesser variability of bed fluctuations in height with respect to the mesoscale. This appears obvious, as the microscale represents the bed at the scale of grains, without the effect of large scale trends. Furthermore, it can be seen a decreasing in the spectral slope (equal to ~ 1.67) only for the unvegetated case (runs R1A and R2A). This confirms that, also at the microscale, the bed structures of comparable energy have a lower height in the absence of the stems.

The statistical analysis of the bed morphology was extended to the investigation of the higher-order structure functions of the fluctuations of the bed surface elevation. In details, we applied the generalized 2D high-order structure functions, as was done by Nikora and Walsh [33], as follows:

$$S_p(l_x, l_y) = \frac{1}{(N-r)} \frac{1}{(M-s)} \sum_{j=1}^{N-r} \sum_{k=1}^{M-s} [|z'(x_j + r\delta x, y_k + s\delta y) - z'(x_j, y_k)|]^p \quad (2)$$

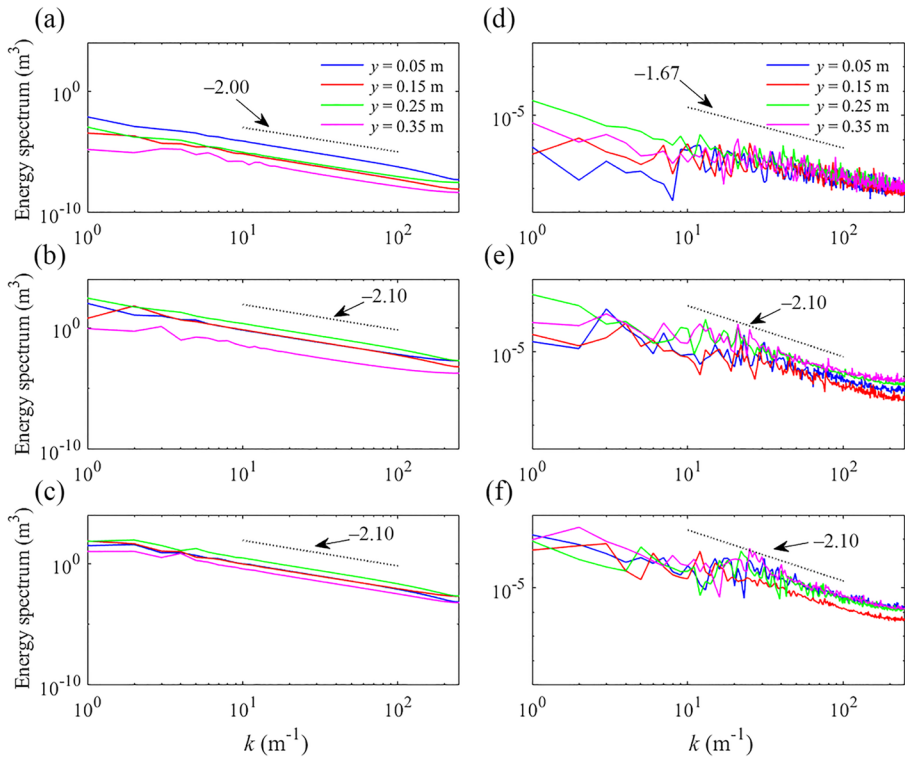


Fig. 14 Energy spectra of the longitudinal bed elevations at $y=0.05, 0.15, 0.25,$ and 0.35 m of runs **a** R1A at the mesoscale, **b** R1B at the mesoscale, **c** R1C at the mesoscale, **d** R1A at the microscale, **e** R1B at the microscale, and **f** R1C at the microscale

In the above equation, p is the order of the moments of the structure functions, l_x is the sampling length in the x direction ($=r\delta x$), l_y is the sampling length in the y direction ($=s\delta y$), $j = 1, 2, 3, \dots, r$, s is the number of samples in the x direction, $k = 1, 2, 3, \dots, s$, s is the number of samples in the y direction, and δx and δy are the sampling intervals in the x and y directions, respectively. In this study, we considered $\delta x = \delta y = 2$ mm.

However, before analyzing the 2D structure functions, the generalized streamwise structure functions were derived from Eq. (2) as $S_p(l_x, l_y = 0)$. In particular, the generalized streamwise structure functions were computed up to the sixth-order, in accordance with Camussi et al. [34] and Nikora and Walsh [33], in order to identify the scaling behavior of $S_p(l_x)$. This latter can be expressed as $S_p(l_x) \sim l_x^{\xi_p}$, where ξ_p is the scaling exponent. In case of a simple scaling, the scaling exponent can be defined as $\xi_p = pH$, where H is the Hurst coefficient describing how the probability density function of the bed elevation fluctuations changes over scales. Instead, for a multiscaling behavior, ξ_p is a nonlinear function of p , i.e. $\xi_p \neq pH$. In this case, more than one parameter is required to describe the behavior of the probability density function changes over scales and the investigated series is called multifractal [27, 35–39].

Figure 16 shows the high-order generalized streamwise structure functions $S_p(l_x)$ at the mesoscale for all the runs. Specifically, Figs. 16a–c refer to runs R1, whereas Figs. 16d–f illustrate the results obtained in runs R2. It is possible to note that the structure functions

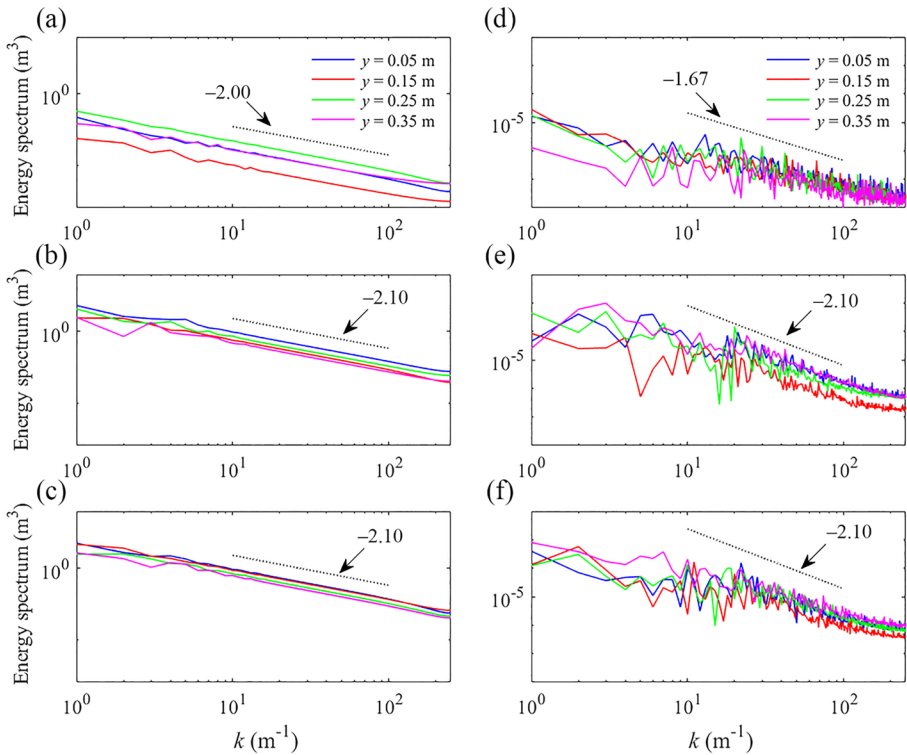


Fig. 15 Energy spectra of the longitudinal bed elevations at $y=0.05, 0.15, 0.25,$ and 0.35 m of runs **a** R2A at the mesoscale, **b** R2B at the mesoscale, **c** R2C at the mesoscale, **d** R2A at the microscale, **e** R2B at the microscale, and **f** R2C at the microscale

can be divided into three ranges of scales, as proposed by Nikora et al. [40]: scaling, transition and saturation regions. The scaling range occurs at small spatial lags, where S_p can be approximated as $l_x^{\xi_p}$. The saturation region is characteristic of large lags, where S_p assumes a constant value. Then, between the scaling and the saturation zones, the transition range is established. All the structure functions approach the saturation region, confirming that the investigated domain is long enough to be statistically investigated. Note that the boundary between the scaling and the transition ranges is of the order of about 0.03 m for run R1A, 0.05 m for run R1B, and 0.07 m for run R1C. Instead, for runs R2A, R2B and R2C, the threshold beyond which the transition region occurs is 0.03, 0.03 and 0.06 m, respectively. Therefore, the scaling region is longer for the runs with a low flow discharge (runs R1), but increases its length as the vegetation density increases. Comparing the high-order generalized structure functions, runs R1C and R2C exhibit narrower transition regions than the other runs. Interestingly, the boundary between the transition and the saturation zones occurs at lower spatial lags in runs R2B and R2C than in the corresponding runs of R1 type, owing to the shorter length scale of the bed undulations with respect to those in R1B and R1C, respectively.

The scaling behavior within the scaling range was investigated by plotting the scaling exponents, ξ_p , as a function of the corresponding order of moments p of the structure functions. Specifically, the scaling exponents were determined for each curve, applying a power

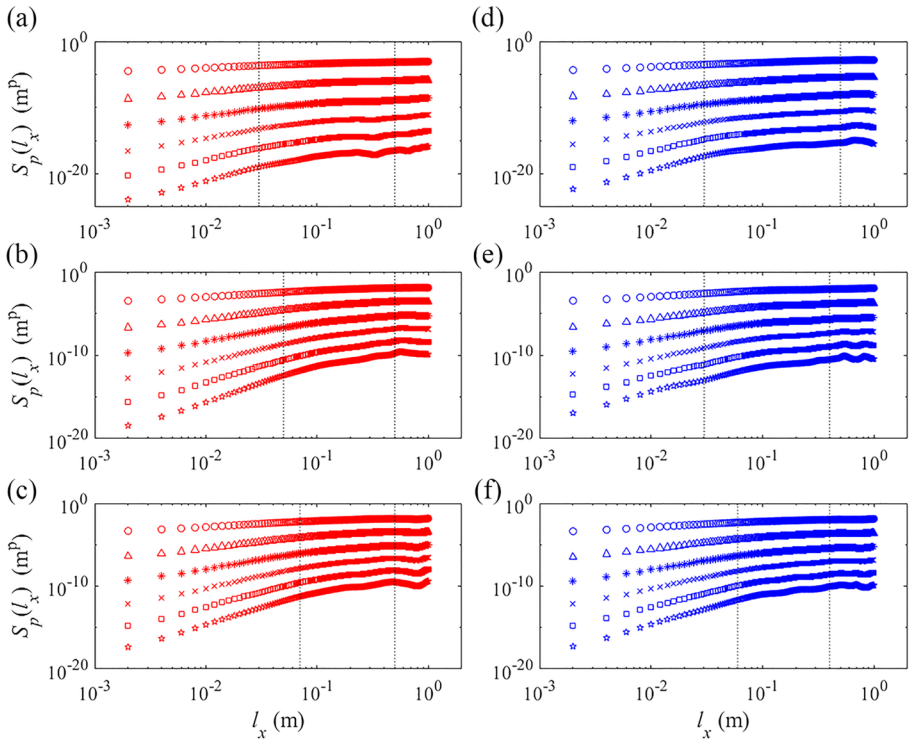


Fig. 16 High-order generalized longitudinal structure functions $S_p(l_x)$ at the mesoscale for runs **a** R1A, **b** R1B, **c** R1C, **d** R2A, **e** R2B, and **f** R2C. The symbol \circ refers to $p=1$, Δ to $p=2$, $*$ to $p=3$, \times to $p=4$, \square to $p=5$, and \star to $p=6$

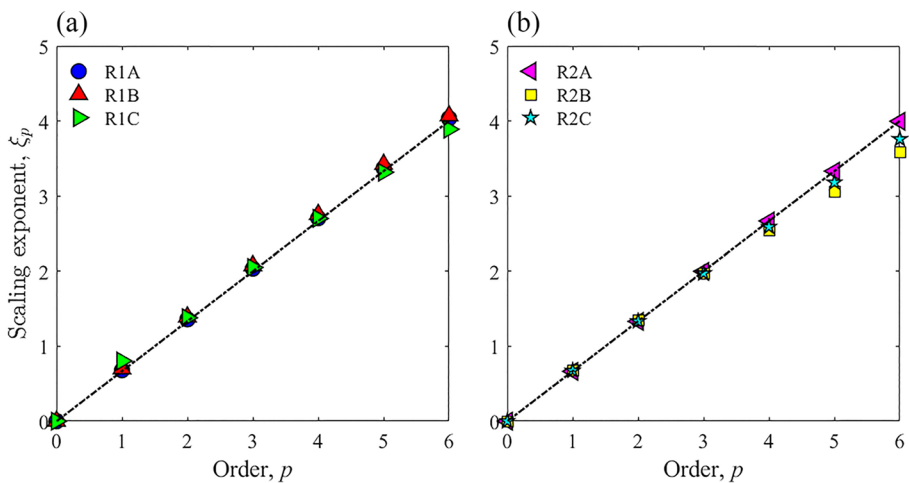


Fig. 17 Scaling exponent ξ_p versus order p of the generalized streamwise structure functions for runs **a** R1A, R1B, R1C, and **b** R2A, R2B, R2C

function to the scaling region for each p order, as shown in Fig. 17. It can be noted that all the runs follow a linear trend, except runs R1C, R2B and R2C (i.e., the dense vegetated flow with a low flow discharge and both the vegetated flows with high flow discharge), which slightly deviate from the linear law. This means that, at small spatial lags, the bed surfaces are simple (or mono-) fractals and can be described by a single exponent. Instead, for runs R1C, R2B and R2C the bed surfaces in the scaling range are characterized by multifractality. This implies slight inhomogeneous arrangement of the local fluctuations in the bed elevations data, which can be attributed to the fact that, as a consequence of bed instability, a complex bed morphology at small spatial lags occurs at the end of runs R1C, R2B and R2C. If the analysis had been limited to the observation of the bed contour plots or of the bed profiles, this particular aspect would have not been perceived. It should be mentioned that precisely runs R1C, R2B and R2C were those affected also by a lateral dispersion of sediments during the sediment transport phase, as was previously discussed analyzing Figs. 6 and 7.

To describe the nonlinear dependence of ξ_p on p , the following polynomial was applied:

$$\xi_p = pH - \frac{C}{2}p^2, \tag{3}$$

where C is the intermittency parameter and the term $-(C/2)p^2$ represents the deviation from the straight line $\xi_p = pH$. Since the scaling behavior of the second-order structure

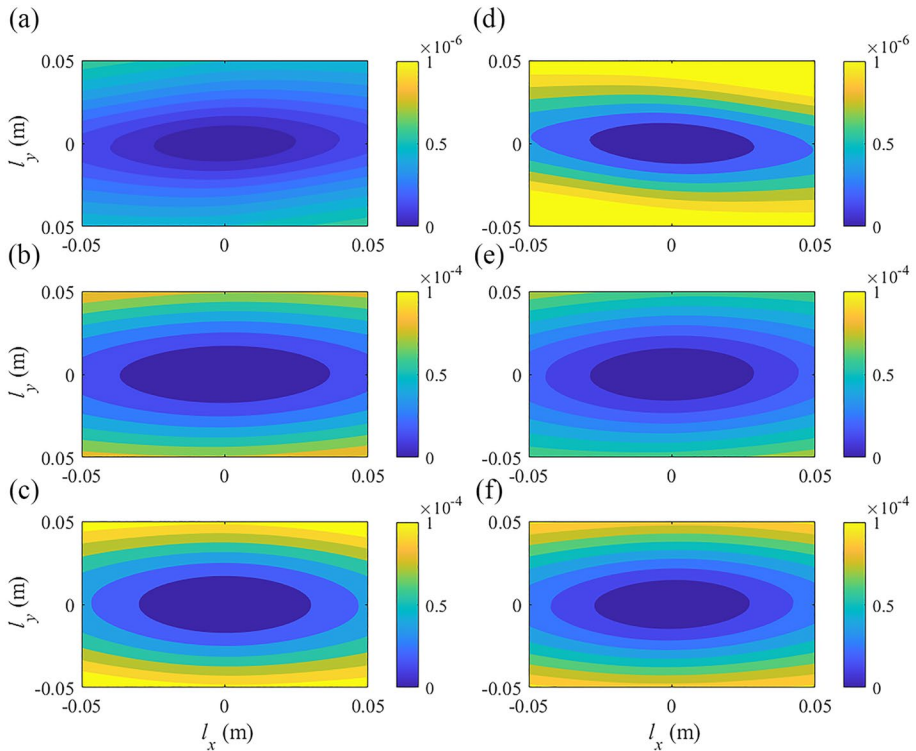


Fig. 18 Contour plots of 2D second-order structure functions $S_2(l_x, l_y)$ at the mesoscale for runs **a** R1A, **b** R1B, **c** R1C, **d** R2A, **e** R2B, and **f** R2C. The colorbars indicate $S_2(l_x, l_y)$ expressed in m^2

functions is consistent with both simple scaling and multiscaling, the Hurst coefficient can be obtained from $S_2(l_x) \sim l_x^{2H}$. Thus, considering that the value of ξ_p at the second order is 1.33, it is possible to derive that the Hurst coefficient is equal to 0.66. Furthermore, the intermittency parameter is equal to 0.02, 0.0005 and 0.003 for runs R2B, R1C and R2C, respectively, whereas the determination coefficient R^2 of the function $\xi_p(p)$ is 99.88, 99.71 and 99.88% for the same runs.

As the last step of the statistical analysis of the bed elevation fluctuations, in Fig. 18 the 2D second-order structure functions $S_2(l_x, l_y)$ at the mesoscale are shown for all the runs. They were zoomed in the area that includes the scaling region identified through the study of the high-order streamwise structure functions ($0.05 \times 0.05 \text{ m}^2$). It can be noted that all the runs are characterized by elliptical contours, which indicate that evidently the changes in bed morphology structures are predominant in the streamwise direction. This means that the bed is characterized by an anisotropic behavior, which reflects the way in which the bed was formed. The principal axes of the ellipses are aligned to the streamwise direction, indicating the development of flow-aligned bed structures. However, some differences can be noted through a detailed analysis of Fig. 18. In fact, for example, one can see that the ellipses of run R2A (Fig. 18d) are more elongated along the x direction than those of run R1A (Fig. 18a). This recalls the bed structures initially observed in Figs. 6 and 7. In the same way it is possible to note that, as expected, the ellipses of run R2B (Fig. 18e) are narrower than those of run R1B (Fig. 18b), since in the latter a slight lateral dispersion of sediments was observed. Finally, the comparison between runs R1C (Fig. 18c) and R2C (Fig. 18f) demonstrates that, by increasing the stem number, the bed structures become shorter than before and they resulted to be laterally expanded. Also in this case and for the same reasons, as previously noted for runs with vegetation of type B, the bed structures are shorter and narrower in run R2C than in run R1C.

6 Conclusions

This study aimed at investigating the effect of streambed instability in vegetated channels. A laboratory flume study was conducted considering two different perturbations in the experimental conditions: a change in (1) vegetation density and (2) flow discharge. Thus, starting from an initial condition in which the bed sediments were stable, owing to an increase in the flow discharge and the presence of vegetation with different densities, the bed became unstable. The consequent sediment transport was originated solely from the erosive action of the flow that caused bed instability. The sediment transport rate was measured during the total duration of each of the six experimental runs performed, that is until a new bed stability condition was achieved. At the end of each experimental run, the bed morphology was captured by a Laser Scanner and the photogrammetry technique, and its changes with the vegetation and flow conditions were investigated. The main concluding findings of this study are summarized below.

The measurements of the sediment transport rate show that this process is thoroughly influenced by the presence of vegetation and its density: it decreases as the vegetation density increases, with much more efficiency in the case of high flow intensity. Thus, the presence of vegetation contributes in promoting the stability of the streambed.

The visual observation of the bed morphology allows verifying the formation of multiple bars in the case of unvegetated rivers, as a result of the erosion and sediment transport processes, that occur owing to the bed instability. However, a more complex bed

morphology is visible at the end of the runs with vegetated flows. In runs with low vegetation density, scour holes, in correspondence of the stems, and dunes have an elongated shape along the streamwise direction, implying that the trajectory of sediment transport is predominantly in the longitudinal direction. However, a slight lateral dispersion of sediments is observed in the run with low flow discharge, owing to a lower flow intensity than in that characterized by a higher flow discharge. By increasing the vegetation density, the bed structures become shorter than before and they result to be laterally expanded, owing to the obstruction created by the stems that originates both longitudinal and lateral sediment transport.

The analysis of the bed longitudinal profiles in terms of elevation fluctuations reveals that those corresponding to vegetated flows with the same density have lower wavelengths in runs R2 (high flow discharge) than in runs R1 (low flow discharge), but they have a very similar trend. This is a sign of a particular phenomenon that occurs recursively for fixed vegetation density, stem diameter and sediment diameter, regardless of the flow discharge. This latter is responsible only for the magnitude of bed degradation and not for the configuration of the bed morphology, which is instead dictated by the vegetation density and distribution. Also the maximum scour depths at the stems are similar between the runs having the same vegetation density. However, they are slightly higher in runs R1, owing to a flow intensity closer to the threshold beyond which the clear-water condition is no longer valid and the erosion occurs with sediment transport. At the same time, the analysis of the bed transverse profiles confirms the presence of multiple bars in the unvegetated flow with high flow discharge. Furthermore, it is possible to observe that the bed undulations in runs with high vegetation density have a shorter wavelength and lower amplitude than those in the runs with low vegetation density.

Concerning the energy spectra and the high-order generalized structure functions, they allow demonstrating and clarifying, from another viewpoint, some important aspects. Firstly, the identification of the characteristic length scales through the energy spectra analysis showed that for the unvegetated flow the increase in the flow discharge causes a stretch of the bed structures at the mesoscale, but the presence of vegetation causes their contraction. At a fixed flow discharge, the shrinking of the bed structures increases as the vegetation density increases. Secondly, the study of the scaling properties of the high-order generalized streamwise structure functions reveals that, at small spatial lags, the bed surfaces are simple (or mono-) fractals and can be described by a single exponent. However, the runs affected also by a lateral dispersion of sediments during the sediment transport phase are characterized by multifractality. This implies slight inhomogeneous arrangement of the local fluctuations in the bed elevations data, which can be attributed to the fact that, as a consequence of bed instability, a complex bed morphology at small spatial lags occurs at the end of these runs. This is an important finding that cannot be perceived through a study based alone on the comparison among the longitudinal bed profiles or the contour plot of the bed surface elevations. Thirdly, the study of the 2D second-order structure functions confirms that for all the runs the changes in bed morphology structures are predominant in the streamwise direction. This means that the bed is characterized by an anisotropic behavior, which reflects the way in which the bed was formed. In fact, as expected, the run with low vegetated density and high flow discharge showed narrower bed structures than those with low flow discharge, as in the latter a slight lateral dispersion of sediments was observed. Furthermore, by increasing the stem number, the bed structures became shorter than before and they resulted to be laterally expanded.

In essence, this study offers an in-depth description of the bed morphology of vegetated flows before and after the passage of a flow discharge that caused its instability. In future experiments, further flow conditions and vegetation density will be investigated. Most of all, particular attention will be paid in describing the time evolution of the identified bed structures. This would permit an accurate description of the effect on the bed morphology of vegetated flows in the bed instability-stability transition.

Acknowledgements The authors thank Ms. Cristiana Piro and Ms. Nicol Innocenza Bonetti, who took part in the experimental activity during their thesis. The authors acknowledge the financial support provided by the “SILA” PONa3_00341 project, “An Integrated System of Laboratories for the Environment”.

Data availability Data are available from the corresponding author by request.

Declarations

Conflict of interest The authors declare that they have no conflict of interests.

Open Access This article is licensed under a Creative Commons Attribution 4.0 International License, which permits use, sharing, adaptation, distribution and reproduction in any medium or format, as long as you give appropriate credit to the original author(s) and the source, provide a link to the Creative Commons licence, and indicate if changes were made. The images or other third party material in this article are included in the article's Creative Commons licence, unless indicated otherwise in a credit line to the material. If material is not included in the article's Creative Commons licence and your intended use is not permitted by statutory regulation or exceeds the permitted use, you will need to obtain permission directly from the copyright holder. To view a copy of this licence, visit <http://creativecommons.org/licenses/by/4.0/>.

References

1. Dey S, Ali SZ (2020) Fluvial instabilities. *Phys Fluids* 32(6):061301
2. Bärenbold F, Crouzy B, Perona P (2016) Stability analysis of ecomorphodynamic equations. *Water Resour Res* 52(2):1070–1088
3. Seminara G (2010) Fluvial sedimentary patterns. *Annu Rev Fluid Mech* 42(1):43–66
4. Olsen DS (1993) Assessing stream channel stability thresholds. Graduate Student Theses, Dissertations, & Professional Papers 7470
5. Schumm SA (1971) Fluvial geomorphology: channel adjustment and river metamorphosis. Water Resources Publications, Highlands Ranch, Colorado
6. Southard JB (1991) Experimental determination of bed-form stability. *Annu Rev Fluid Mech* 19(1):423–455
7. Charru F, Andreotti B, Claudin P (2013) Sand ripples and dunes. *Annu Rev Fluid Mech* 45:469–493
8. Maji S, Hanmaiahgari PR, Balachandar R, Pu JH, Ricardo AM, Ferreira RML (2020) A review on hydrodynamics of free surface flows in emergent vegetated channels. *Water* 12(4):1218
9. D'Ippolito A, Calomino F, Alfonsi G, Lauria A (2021) Flow resistance in open channel due to vegetation at reach scale: a review. *Water* 13(2):116
10. Gurnell AM, Bertoldi W, Corenblit D (2012) Changing river channels: The roles of hydrological processes, plants and pioneer fluvial landforms in humid temperate, mixed load, gravel bed rivers. *Earth Sci Rev* 111(1):129–141
11. Camporeale C, Perucca E, Ridolfi L, Gurnell A (2013) Modeling the interactions between river morphodynamics and riparian vegetation. *Rev Geophys* 51(3):379–414
12. Nepf HM, Vivoni ER (2000) Flow structure in depth-limited, vegetated flow. *J Geophys Res Oceans* 105(C12):28547–28557
13. Vastila K, Järvelä J (2014) Modeling the flow resistance of woody vegetation using physically based properties of the foliage and stem. *Water Resour Res* 50(1):229–245
14. Penna N, Coscarella F, D'Ippolito A, Gaudio R (2020) Bed roughness effects on the turbulence characteristics of flows through emergent rigid vegetation. *Water* 12(9):2401
15. Coscarella F, Penna N, Ferrante AP, Gualtieri P, Gaudio R (2021) Turbulent flow through random vegetation on a rough bed. *Water* 13(18):2564

16. López F, García M (1998) Open-channel flow through simulated vegetation: Suspended sediment transport modeling. *Water Resour Res* 34(9):2341–2352
17. Nepf HM (2012) Flow and Transport in Regions with Aquatic Vegetation. *Annu Rev Fluid Mech* 44(1):123–142
18. Wu H, Cheng NS, Chiew YM (2021) Bed-load transport in vegetated flows: phenomena, parametrization, and prediction. *Water Resour Res* 57(4):e2020WR028143z
19. Tang H, Wang H, Liang DF, Lv SQ, Yan L (2013) Incipient motion of sediment in the presence of emergent rigid vegetation. *J Hydro-Environ Res* 7(3):202–208
20. Yang JQ, Chung H, Nepf HM (2016) The onset of sediment transport in vegetated channels predicted by turbulent kinetic energy. *Geophys Res Lett* 43:11261–11268
21. Armanini A, Cavedon V (2019) Bed-load through emergent vegetation. *Adv Water Resour* 129(July):250–259
22. Dey S, Sarkar A (2006) Scour downstream of an apron due to submerged horizontal jets. *J Hydraul Eng* 132(3):246–257
23. Neill CR (1973) Guide to bridge hydraulics. University of Toronto Press (Toronto, Canada) p 191
24. Mueller DS, Wagner CR (2005) Field observations and evaluations of streambed scour at bridges. Report no. FHWA–RD–03–052 US Department of Transportation, Federal Highway Administration (Washington, DC, USA)
25. Bertin S, Friedrich H (2014) Measurement of gravel-bed topography: evaluation study applying statistical roughness analysis. *J Hydraul Eng* 140(3):269–279
26. Bertin S, Groom J, Friedrich H (2017) Isolating roughness scales of gravel-bed patches. *Water Resour Res* 53(8):6841–6856
27. Penna N, Padhi E, Dey S, Gaudio R (2021) Statistical characterization of unworked and water-worked gravel-bed roughness structures. *J Hydraul Res* 59(3):420–436
28. Marion A, Tait SJ, McEwan IK (2003) Analysis of small-scale gravel bed topography during armor-ing. *Water Resour Res* 39(12):1334
29. Bertin S, Friedrich H (2018) Effect of surface texture and structure on the development of stable fluvial armors. *Geomorphology* 306(April):64–79
30. Melville BW, Coleman SE (2000) Bridge scour. Water Resources Publication, Littleton
31. Priestley MB (1981) Spectral analysis and time series: probability and mathematical statistics. Academic Press, Cambridge
32. Ferraro D, Lauria A, Penna N, Gaudio R (2021) Temporal development of unconfined propeller scour in waterways. *Phys Fluids* 33(9):095119
33. Nikora V, Walsh J (2004) Water-worked gravel surfaces: High-order structure functions at the particle scale. *Water Resour Res* 40(12):W12601
34. Camussi R, Baudet C, Benzi R, Ciliberto S (1996) Statistical uncertainty in the analysis of structure functions in turbulence. *Phys Rev E* 54(4):R3098–R3101
35. Castaing B, Gagne Y, Hopfinger EJ (1990) Velocity probability density functions of high Reynolds number turbulence. *Phys D* 46(2):177–200
36. Venugopal V, Roux SG, Fofoula-Georgiou E, Arneodo A (2006) Revisiting multifractality of high-resolution temporal rainfall using a wavelet based formalism. *Water Resour Res* 42(6):W06D14
37. Singh A, Fienberg K, Jerolmack DJ, Marr J, Fofoula-Georgiou E (2009) Experimental evidence for statistical scaling and intermittency in sediment transport rates. *J Geophys Res* 114(F1):F01025
38. Singh A, Guala M, Lanzoni S, Fofoula-Georgiou E (2012) Bedform effect on the reorganization of surface and subsurface grain size distribution in gravel bedded channels. *Acta Geophys* 60(6):1607–1638
39. Coscarella F, Penna N, Servidio S, Gaudio R (2020) Turbulence anisotropy and intermittency in open-channel flows on rough beds. *Phys Fluids* 32(11):115127
40. Nikora VI, Goring DG, Biggs BJB (1998) On gravel bed roughness characterization. *Water Resour Res* 34(3):517–527

Publisher's Note Springer Nature remains neutral with regard to jurisdictional claims in published maps and institutional affiliations.